5666 *Biochemistry* **1999,** *38,* 5666−5675

A Model for the Solution Structure of Oxidized Terpredoxin, a Fe_2S_2 Ferredoxin from *Pseudomonas*[†,‡]

Huaping Mo,[§] Susan Sondej Pochapsky,[||] and Thomas C. Pochapsky*,[§]

Department of Chemistry, Brandeis University, Waltham, Massachusetts 02454, and Francis Bitter Magnet Laboratory, Massachusetts Institute of Technology, Cambridge, Massachusetts 02139

Received December 29, 1998; Revised Manuscript Received February 24, 1999

ABSTRACT: Terpredoxin (Tdx) is a 105-residue bacterial ferredoxin consisting of a single polypeptide chain and a single Fe_2S_2 prosthetic group. Tdx was first identified in a strain of *Pseudomonas sp*. capable of using α-terpineol as sole carbon source. The Tdx gene, previously cloned from the plasmid-encoded *terp* operon, that carries genes encoding for proteins involved in terpineol catabolism, has been subcloned and expressed as the holoprotein in *E. coli*. Physical characterization of the expressed Tdx has been performed, and a model for the solution structure of oxidized Tdx (Tdx^o) has been determined. High-resolution homo- and heteronuclear NMR data have been used for structure determination in diamagnetic regions of the protein. The structure of the metal binding site (which cannot be determined directly by NMR methods due to paramagnetic broadening of resonances) was modeled using restraints obtained from a crystal structure of the homologous ferredoxin adrenodoxin (Adx) and loose restraints determined from paramagnetic broadening patterns in NMR spectra. Essentially complete ^1H and ^{15}N NMR resonance assignments have been made for the diamagnetic region of Tdx^o (ca. 80% of the protein). A large five-stranded β-sheet and a smaller two-stranded β-sheet were identified, along with three α-helices. A high degree of structural homology was observed between Tdx and two other ferredoxins with sequence and functional homology to Tdx for which structures have been determined, Adx and putidaredoxin (Pdx), a homologous *Pseudomonas* protein. $^1H/^2H$ exchange rates for Tdx backbone NH groups were measured for both oxidation states and are rationalized in the context of the Tdx structure. In particular, an argument is made for the importance of the residue following the third ligand of the metal cluster (Arg49 in Tdx, His49 in Pdx, His56 in Adx) in modulating protein dynamics as a function of oxidation state. Some differences between Tdx and Pdx are detected by UV−visible spectroscopy, and structural differences at the C-terminal region were also observed. Tdx exhibits only 2% of the activity of Pdx in turnover assays performed using the reconstituted camphor hydroxylase system of which Pdx is the natural component.

The cytochromes P450 are widely distributed in nature, with examples having been isolated from bacteria, plants, and animals. These enzymes typically catalyze the insertion of one oxygen atom from O_2 into an inactivated C−H bond while reducing the second oxygen atom to water. Two electrons, usually obtained by oxidation of a reducing nucleotide such as NADH or NADPH, are required for each turnover. Detoxification of xenobiotics and steroid biosynthesis are some of the many biochemical pathways that involve cytochromes P450. There are two recognized classes of cytochromes P450. Type I cytochromes P450 are reduced directly by the flavoprotein that binds the nucleotide, the electrons being transferred directly from the nucleotide-bound flavoprotein to the cytochrome. In type II catalytic cycles, a ferredoxin acts as an electron shuttle between the flavoprotein and the cytochrome.

The archetype of type II cytochrome P450s, cytochrome $P450_{cam}$ (CYP101), catalyzes the stereospecific hydroxylation of camphor in *Pseudomonas putida* in the course of camphor catabolism by a strain of the bacterium capable of using camphor as sole carbon and energy source (*1*). The camphor hydroxylase enzyme system consists of three proteins, putidaredoxin reductase (PdR), putidaredoxin (Pdx),[1] and CYP101. Recently, a similar hydroxylase has been identified in another strain of *Pseudomonas* capable of using α-terpineol as sole carbon source (*2*, *3*). Like the camphor hydroxylase, the terpineol hydroxylase system consists of three proteins: terpredoxin reductase (TdR), the Fe_2S_2 ferredoxin

---

[†] This work was supported in part by a grant from the National Institutes of Health (GM44191, T.C.P.). S.S.P. acknowledges support from Grant P41-RR00995 (MIT FBML).

[‡] A set of 15 structures have been deposited with the Brookhaven PDB database with the access code 1b9r.

[§] Brandeis University.

[||] Massachusetts Institute of Technology.

[1] Abbreviations: 2D, two-dimensional; 3D, three-dimensional; Adx, adrenodoxin; COSY, correlation spectroscopy; DQ, double quantum; DQF, double quantum filter; DSS, 2,2-dimethyl-2-silapentane-5-sulfate; DTT, dithiothreitol; HSQC, heteronuclear single quantum correlation; IPTG, isopropyl β-thiogalactoside; MALDI-TOF, matrix-assisted laser desorption ionization time-of-flight; NMR, nuclear magnetic resonance; NOE, nuclear Overhauser effect; NOESY, NOE spectroscopy; OD, optical density; Pdx, putidaredoxin; PCR, polymerase chain reaction; SDS−PAGE, sodium dodecyl sulfate−polyacrylamide gel electrophoresis; TOCSY, total correlation spectroscopy; Tdx, terpredoxin; TPPI, time proportional phase increment; WATERGATE, water suppression by gradient-tailored excitation.

10.1021/bi983063r CCC: $18.00

terpredoxin (Tdx), and cytochrome P-450$_{terp}$ (CYP108). CYP108 catalyzes the 7-hydroxylation of α-terpineol, the first step of α-terpineol's uptake by *Pseudomonas*.

Despite a high degree of functional and sequence similarities between corresponding proteins in the two bacterial hydroxylase pathways, the ferredoxins (Tdx and Pdx) show low cross-reactivity when substituting for each other in their respective pathways. Pdx can replace Tdx in terpineol hydroxylation but only with 10% efficiency (*4*), and the maximum efficiency of Tdx in the reconstituted camphor hydroxylase system is around 2% (H. Gong, unpublished results). It is likely that there is a structural basis for this specificity involving one or both of the redox partners in both systems. This requires that the structures of all of the redox partners be determined in order to identify the structural features involved in binding and electron transfer. The structures of both CYP101 and CYP108 have been solved crystallographically (*5*, *6*), and we have described a model for the solution structure of oxidized Pdx based on NMR-derived restraints and modeling of the paramagnetic Fe_2S_2 binding region (*7*, *8*). Recently, the structure of a C-terminal truncation mutant of adrenodoxin (Adx), a mammalian ferredoxin that serves as reductant for mammalian cytochromes P450 involved in steroid biosynthesis, was determined crystallographically (*9*). The Pdx and Adx structures show considerable similarity, with a 1.64 Å RMS difference between homologous backbone atoms in Adx and the average solution structure of Pdx. We now describe a NMR-derived model for the solution structure of oxidized terpredoxin (Tdx^{o}). In our analysis, we compare the Tdx structure with those of Pdx and Adx and interpret these comparisons in terms of structure−function relationships in the three enzyme systems.

MATERIALS AND METHODS

Protein Expression, Purification, and NMR Sample Preparation. Preliminary two-dimensional ^{1}H NMR experiments on Tdx^{o} were performed using samples of Tdx purified from *Pseudomonas* grown using α-terpineol as sole carbon source (*2*). However, to obtain sufficient Tdx for extensive NMR and biophysical studies, overexpression in *E. coli* was necessary. The Tdx gene was originally cloned into the cloning vector PCRII (J. A. Peterson, private communication), with the Tdx gene flanked by two *EcoRI* sites. Using polymerase chain reaction (PCR), an *NdeI* site was introduced at the N-terminal end of the Tdx gene, which allowed the gene to be inserted into an expression vector, pET-23a (*10*), between the *NdeI* and *EcoRI* sites in the correct orientation and position for induced expression. The T7 tag for the pET-23a vector was deleted in this construct (pHM1) in order to avoid possible disruption of folding of the expressed ferredoxin. pET-23a contains a T7 terminator downstream of the polylinker region, which prevents readthrough by T7 polymerase.

Expression of the Tdx gene encoded in pHM1 was accomplished in *E. coli* strain BL21(DE3) *PlysS* (Novogen). Cells were grown initially in Luria−Bertani medium and then transferred to M9 minimal medium (*11*) supplemented with 30 μM $FeCl_3$. Isopropyl β-thiogalactoside (IPTG, final concentration 0.4 mM) was used to induce expression after a cell density $OD_{600\ nm} = 1$ was reached; 200 μg/mL ampicillin (Sigma) and 34 μg/mL chloramphenicol (ICN Biomedical Inc.) were added to ensure that antibiotic pressure was maintained during growth. For preparation of uniformly ^{15}N-labeled Tdx, $^{15}NH_4Cl$ (CIL) was used as sole nitrogen source in the growth medium. Cell pellets were harvested overnight after induction and stored in a −70 °C freezer. It was found that induction with IPTG after the OD reaches 1.0 or higher gives the highest yield of protein.

Ten grams of cell pellets, either freshly obtained or from frozen stock, was lysed overnight by treatment with 0.1 g of hen egg lysozyme (Sigma) in the presence of 3 mg of RNase I, 3 mg of DNase I (Sigma), and 8 mg of toluenesulfonyl chloride (Sigma) as protease inhibitor in 40 mL of cold-degassed and N_2-saturated 50 mM Tris-HCl buffer (pH 8.0) containing 2 mM DTT. The lysis mixture was then sonicated and the supernatant liquid (which contains Tdx) clarified by centrifugation. If desired, the cell pellets recovered from the centrifugation could be treated in order to recover unfolded or misfolded apo-Tdx, which could then be reconstituted to holo-Tdx (*12*−*14*).

The supernatant liquid containing the Tdx was loaded onto a DEAE anion exchange column (20 mL, Whatman DE52) preequilibrated with degassed 50 mM Tris-HCl (2 mM DTT, pH 8.0) buffer. A linear gradient of 0−0.6 M KCl, also in degassed 50 mM Tris-HCl (2 mM DTT, pH 8.0) buffer, was applied to the loaded DEAE column. Tdx was eluted at high-salt buffer (ca. 0.3 M KCl) from the column. The red-colored fractions containing Tdx were then pooled and concentrated to less than 1 mL in total volume. The concentrated protein was loaded in a narrow band onto a P-30 (BioRad) gel exclusion column (100 mL) preequilibrated with 50 mM Tris-HCl/2 mM DTT, pH 7.4. The same buffer was used to elute the Tdx from the column, with the flow rate determined by a 70 cm hydrostatic pressure difference across the column. Fractions with absorbance ratio A_{460}/A_{280} greater than 0.54 were considered sufficiently pure for NMR spectroscopy and other purposes. Recombinant and/or reconstituted Tdx was shown to be equivalent to that isolated from *Pseudomonas* by comparison of 1D and 2D NMR spectra, UV−visible spectroscopy, and mobility on SDS−PAGE protein gels.

Buffer exchange for most NMR experiments was accomplished using a P-2 (BioRad) spin column preequilibrated with buffer containing 9:1 H_2O/D_2O and 50 mM perdeuterated Tris-HCl (CIL), pH 7.4, or in the same buffer (pH 7.4, uncorrected for isotope effect) made up using 99.9% D_2O. Both buffers contained 2 mM DTT as a preservative. A typical Tdx concentration for an NMR sample was ca. 3 mM.

NMR Spectroscopy. NMR experiments were performed either on a Bruker AMX500 11.74 T (500 MHz ^{1}H) NMR (Brandeis University) or on a home-built 17.6 T (750 MHz ^{1}H) NMR at the Francis Bitter Magnet Laboratory (Massachusetts Institute of Technology). The AMX500 is equipped with three RF channels, a three-channel pulsed field gradient amplifier, and a three-axis gradient triple resonance inverse detection probe. The FBML 750 MHz NMR is equipped with a single-axis gradient and inverse detection probe. All NMR experiments were performed at 290 K with recovery delays ranging from 0.7 to 1.2 s. ^{1}H chemical shifts were externally referenced to DSS. ^{15}N chemical shifts were indirectly referenced to ^{1}H using a proportionality of gyromagnetic ratios (^{15}N/^{1}H) of 0.101329118 (*15*). Quadrature detection in indirect dimensions for all 2D and 3D experiments (except for the J dimension of 3D J_{HNHA}-resolved $^{1}H,^{15}N$ HSQC) was achieved either by TPPI (*16*) or by States-TPPI (*17*).

Standard homonuclear ^{1}H 2D NMR experiments were performed, including DQF-COSY (*18*, *19*), NOESY (*20*) using either water flip-back (*21*) and WATERGATE (*22*, *23*) or presaturation for water suppression, TOCSY (*24*), and double quantum experiments (*25*). NOESY experiments were performed using a 70 ms NOE mixing time. TOCSY experiments were performed using a 70 ms DIPSI-2 spin-lock sequence (7.5 kHz B_1 field) (*26*). A total mixing time of 22.5 ms was used in the homonuclear double quantum experiment. In the direct detect dimension (ω_2) of ^{1}H homonuclear 2D experiments, 2048 complex points were acquired for a spectral width of 7042 Hz at 11.74 T or 10 500 Hz at 17.6 T. In the indirect dimension (ω_1), either 256 or 400 complex points or the TPPI equivalent were collected using the same spectral widths as in the directly detected dimension.

$^{1}H,^{15}N$ HSQC experiments (*27*) were performed using either presaturation or WATERGATE antiselective pulses for water suppression. ^{15}N-edited 3D NOESY−HSQC (*28*) and TOCSY−HSQC experiments were performed at 11.74 and 17.6 T. Spectral width in both proton dimensions was 6029 Hz (11.74 T) or 10 500 Hz (17.6 T) while the ^{15}N dimension was 2027 Hz (11.74 T) or 3000 Hz (17.6 T). All ^{15}N-edited NOESY−HSQC experiments used a NOESY mixing time of 70 ms. A 70 ms spin lock was also used for ^{15}N-edited 3D TOCSY−HSQC experiments in order to facilitate spin system assignments. A short (22 ms) mixing time was used in one ^{15}N-edited TOCSY−HSQC in order to make stereospecific assignment of β-CH_2 protons and to determine restraints on χ_1 dihedral angles (*29*). In all experiments involving ^{15}N, the directly detected ^{1}H dimension used 512 complex points while the indirectly detected ^{1}H dimension consisted of 50−128 points. All 3D experiments consisted of either 16 or 32 complex points in the ^{15}N dimension.

3D J_{HNHA}-resolved $^{1}H,^{15}N$ HSQC, HNHA (*29*, *30*), and HNHB (*29*, *31*) experiments were all performed at 11.74 T. All experiments were acquired with 512 complex points in the direct detect dimension (ω_2) using a 7042 Hz spectral width for the 3D *J*-resolved HSQC experiment and 6024 Hz for both the HNHA and HNHB experiments. The *J*-resolved HSQC data set was collected with spectral widths of 2027 Hz (32 complex points) in the ^{15}N dimension and 40 Hz (16 increments) for the *J* dimension. The indirectly detected ^{1}H dimensions of both the HNHA and HNHB experiments are the same spectral widths as the directly detected dimensions. The ^{15}N dimensions for HNHA and HNHB were set to spectral widths of 2027 Hz (20 complex points for HNHA and 50 complex points for HNHB).

Amide H/D exchange in D_2O was measured by $^{1}H,^{15}N$ HSQC using uniformly ^{15}N-labeled Tdx^{o} as described previously for Pdx^{o} (*32*). Exchange was initiated by passage of Tdx^{o} dissolved in protonated buffer into deuterated buffer of the same ionic strength and pH (uncorrected for isotope effects).

2D NMR homonuclear datasets were processed and analyzed as described previously for Pdx^{o} (*32*, *33*) using Felix97 software (Molecular Simulations, Inc.). 3D datasets were processed using nmrPipe (Molecular Simulations, Inc.) and exported to Felix97 for analysis. All dimensions were zero-filled to increase the number of data points by at least a factor of 2. In the directly detected dimension (t_3), an 80°-shifted sine bell was applied prior to Fourier transformation. In indirectly detected dimensions (t_1 and t_2), an 80°-shifted sine bell was applied, and time-domain data were zero-filled to 128 or 256 complex points (^{1}H) and 64 complex points (^{15}N).

Volume integrals for hydrogen−deuterium (H/D) exchange experiments were measured for corresponding peaks on each time-point $^{1}H,^{15}N$ HSQC spectrum using the integration subroutine of Felix 97, and the volumes fitted to $I = I_0 \exp(-kt) + c$, where I is the integral intensity of a peak at time t, I_0 is the intensity of the same peak in the first experiment ($t = 0$), and c is a constant introduced to correct for base line offset in the integration and residual signal.

Structure Calculations. Structure calculations were performed using X-PLOR 3.851 (A. Brunger, Yale University) operating on a Silicon Graphics O2 workstation. A combined distance geometry-simulated annealing protocol (34) was used with modifications as recently described for Pdx^{o} (*8*). Only bond, angle, NOE, and dihedral and van der Waals energies were used to determine structure energies. No electrostatic terms were used in any of the calculations. Acceptable structures were selected for low overall energies, no NOE violations larger than 0.5 Å, no dihedral violations greater than 5°, ordered secondary structure, and few outliers on the Ramanchandran diagram. Typically, ca. 15 acceptable structures were generated per 100 distance-geometry substructures. Tables 1 and 2 list parameters pertinent to the structural calculations.

RESULTS

Spectrometric and Electrophoretic Characterization of Recombinant Tdx^{o}. As noted above, the recombinant Tdx^{o} used for most of the NMR experiments described here is spectroscopically and electrophoretically identical to Tdx^{o} isolated from the natural source (*Pseudomonas sp.*). MALDI-TOF mass spectra of recombinant Tdx confirm that the product of recombinant expression is of the mass expected (11 097 daltons; M. Heinsen, unpublished results) for the peptide sequence shown in Figure 1. Four absorption maxima are observed spectrophotometrically for Tdx^{o}, with λ_{max} values at 280, 340, 415, 460, and 540 nm (weak). The extinction coefficient at 280 nm was determined to be ~11 cm^{-1} mM^{-1}. Extinction coefficients of other bands were calculated as 8.4 (340 nm), 7.0 (415 nm), 6.3 (460 nm), and 4.0 cm^{-1} mM^{-1} (540 nm). Since Tdx contains only four aromatic residues (as opposed to six found in Pdx), the 415 and 460 nm bands are more pronounced relative to the 280 nm band than in the Pdx^{o} spectrum. Both the 415 and 460 nm bands can be used to judge protein expression, purity, and metal incorporation. Interestingly, Tdx^{o} isolated from either source exhibits a slightly redder color to the eye than Pdx^{o}, which is a chocolate brown. The only feature from the UV−visible spectrum of Tdx^{o} to account for this difference, which is otherwise typical for a $Cys_4Fe_2S_2$ ferredoxin, appears to be a slight broadening of the 340 nm band relative to the same band in Pdx. Reduction of Tdx by $Na_2S_2O_4$ results in the disappearance of the 415 and 460 nm bands, while the 340 nm band is greatly enhanced (Figure 2).

Tdx has a large net negative charge, with a total of 18 acidic residues (8 Asp and 10 Glu) and only 4 positively

Table 1: Modeling Restraints on the Iron−Sulfur Binding Site Residues in Tdx^o

(A) Ligand Restraints for the Fe$_2$S$_2$ Cluster[a]

	distance (Å)		angle (deg)
Cα (Cys39)−Cα (Cys45)	6.0 ± 0.7	Fe−S−Cβ	109.5
Cα (Cys39)−Cα (Cys48)	8.9 ± 0.7	S−Fe−S	105.0
Cα (Cys39)−Cα (Cys86)	9.6 ± 0.7	Fe−S−Fe	75
Cα (Cys45)−Cα (Cys48)	7.7 ± 0.7	N−Cα−Cβ−Sγ (Cys39)	92 ± 20
Cα (Cys45)−Cα (Cys86)	10.1 ± 0.7	N−Cα−Cβ−Sγ (Cys45)	76 ± 20
Cα (Cys48)−Cα (Cys86)	6.3 ± 0.7	N−Cα−Cβ−Sγ (Cys48)	64 ± 20
		N−Cα−Cβ−Sγ (Cys86)	67 ± 20
		Cα−Cβ−Sγ−Fe1 (Cys39)	−85 ± 20
		Cα−Cβ−Sγ−Fe1 (Cys45)	−48 ± 20
		Cα−Cβ−Sγ−Fe2 (Cys48)	−134 ± 20
		Cα−Cβ−Sγ−Fe2 (Cys86)	−116 ± 20

(B) Dihedral Angles (deg) for Relevant Residues Close to the Metal Cluster[b]

	Glu38	Cys39	Gly40	Gly41	Ser42	Cys43	Val44	Cys45	Ala46
φ	−55	−81	63	77	−99	61	−125	−151	−136
ψ	−55	4	37	24	12	40	13	−173	28

	Thr47	Cys48	Arg49	Leu84	Ser85	Cys86	Gln87
φ	−73	−96	−52	−83	−52	−74	−99
ψ	−14	12		114	−31	−10	−1

[a] Bond lengths for Fe-S and Fe-Fe are 2.20 and 2.7 Å, respectively. [b] The maximum allowed deviation is +40°.

Table 2: Restraints Used for Tdx^o Structure Calculations As Described under Materials and Methods

NOEs and paramagnetic restraints		dihedral restraints	
interresidue NOEs		φ	65
long range ($|i - j| > 3$)	390	χ_1	47
short range ($3 \geq |i - j|$)	524	χ_2	1
total	914	Gly (see text)	7
nontrivial intraresidue NOEs	117		
total NOEs	1031	total dihedral restraints	120
paramagnetic restraints	5		

```
      1                                     21
Pdx   * S K V V Y V S H D G T R R E L D V A D G V S L M Q A A V S N G I * Y D I V G D
Tdx   * P R V V F I D E Q S G E Y A V D A Q D G Q S L M E V A T Q N G V * P G I V A E
Adx   K I T V H F I N R D G E T L T T K G K I G D S L L D V V V Q N N L D I D G F G A

      40                                    60
Pdx   C G G S A S C A T C H V Y V N E A F T D K V P A A N E R E I G M L E C V T A E L
Tdx   C G G S C V C A T C R I E I E D A W V E I V G E A N P D E N D L L Q S T G E P M
Adx   C E G T L A C S T C H L I F E Q H I F E K L E A I T D E E N D M L D * L A Y G L

      80                                    100
Pdx   K P N S R L C C Q I I M T P E L D G I V V D V P D R Q W
Tdx   T A G T R L S C Q V F I D P S M D G L I V R V P L P A *
Adx   T D R S R L G C Q I C L T K A M D N M T V R V P D A V S
```

FIGURE 1: Sequence alignment of Pdx (SwissProt PUTX_PSEPU), Tdx (SwissProt TERP_PSESP), and bovine Adx (SwissProt ADX2_BOVIN) using the Needlman and Wunsch algorithm (*58*). An asterisk respresents a gap in the alignment. Pdx shows a 36% identity and 57% similarity with Tdx, and Adx shows a 26% identity and 43% similarity with Tdx.

charged residues (all Arg). Tdx contains no Lys or His. This charge imbalance may be why there are problems with gel electrophoretic characterization of Tdx with SDS−PAGE. Our attempts to use SDS−PAGE gel electrophoresis to monitor and optimize Tdx expression were unsuccessful. Presumably, the large number of negative charges hinders the binding of SDS to the protein, leading to a diffuse band on the gel. Similar behavior has been reported for other acidic ferredoxins (*34*, *35*).

^{1}H and ^{15}N Resonance Assignments. The high degree of sequence homology between Tdx and Pdx (Figure 1) suggests that they share similar secondary and tertiary structures. In fact, many amino acid residues in Tdx exist in very similar environments (as reflected by chemical shift) to corresponding residues in Pdx. For example, Arg83's NϵH has a chemical shift of 10.29 ppm, identical to its counterpart in Pdx (Arg83). Furthermore, patterns of ring current shifts from aromatic rings of Phe5 (Tyr5 in Pdx) and Trp56 (Phe56 in Pdx) to nearby residues are very similar between the two proteins. For this reason, sequential ^{1}H and ^{15}N diamagnetic resonance assignments could be made fairly easily in Tdx^o using homonuclear two-dimensional and ^{1}H,^{15}N TOCSY−HSQC and NOESY−HSQC data sets. Stereospecific ^{1}H assignments for diastereotopic methylene groups were made primarily using ^{1}H,^{15}N NOESY−HSQC, a short mixing time TOCSY, HNHB, and DQ data (*29*). Figure 3 is a ^{1}H,^{15}N HSQC experiment showing the assignments of unique H−N couplings in Tdx^o.

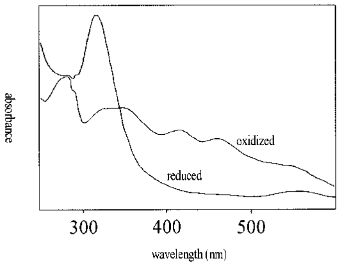

FIGURE 2: UV−visible spectra of oxidized and reduced Tdx. Absorption maxima and extinction coefficients are described in the text.

The lack of *J*-couplings from the C$_\epsilon$H$_3$ methyl resonance of methionine prevents assignments of such signals based on scalar connectivity. ^{1}H assignments were made for Met78 and Met94 C$_\epsilon$H$_3$ signals based on the narrow line shapes, NOEs to resonances from nearby protons and from a natural-abundance ^{1}H,^{13}C HSQC spectrum of Tdx^o, as the C$_\epsilon$H$_3$ correlations are seen in a distinctive region of that 2D spectrum (H. Mo, unpublished results).

The current assignments provide information relevant to the expressed amino acid sequence of Tdx. The nucleotide sequence of the Tdx gene indicates that residue 17 of Tdx is an alanine, while chemical sequencing identifies residue 17 as aspartate (*2*). The NMR assignment process confirms that residue 17 is alanine. There is no evidence for the

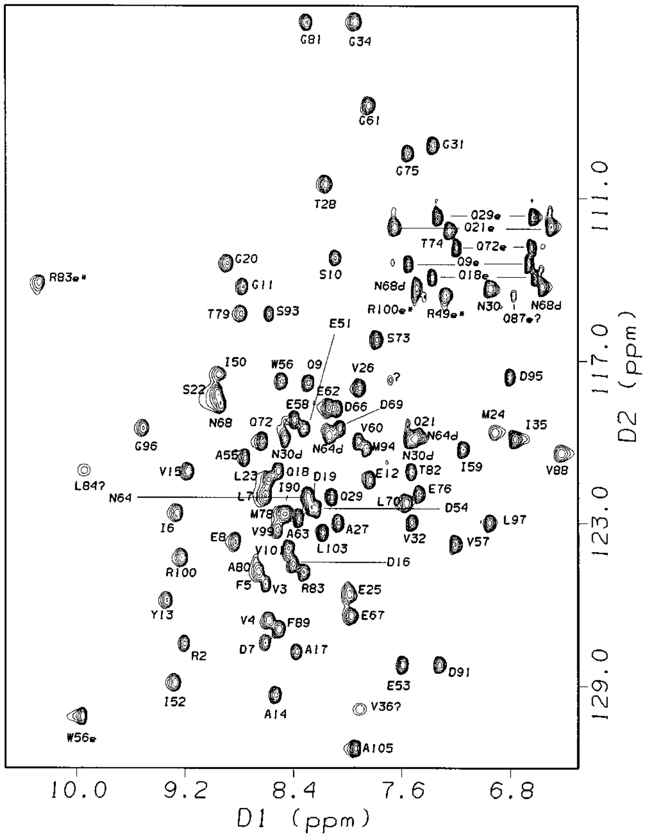

FIGURE 3: 500 MHz (^{1}H) ^{1}H,^{15}N HSQC spectrum of Tdx^o, 290 K (3 mM protein, 50 mM Tris-HCl-d_6, pH 7.4, 2 mM DTT, H_2O/D_2O = 9/1) annotated with the residue number to which the NH correlation is assigned. Cross-peaks with " ? " are tentative (if a residue number is shown) or are unassigned. Peaks marked with an asterisk are folded in the ^{15}N dimension.

presence of an N-terminal methionine in the folded protein, which is listed as Met1 in the published sequence (*2*). The next residue in the sequence, Pro, is the first residue in the sequence observed by NMR (Swiss-Prot ID: TERP_PSESP). For this reason, the numbering system used in the present work starts at the same point as the Pdx sequence (see Figure 1), and homologous residues in Pdx and Tdx have the same sequence number.

Experimental Restraints for Structure Calculations. Experimental and modeling restraints used in the calculations of the solution structures of Tdx^o are summarized in Table 1. NOE intensities were defined as very strong, strong, medium, and weak, corresponding to a distance range of 1.8−2.5 Å, 1.8−3.3 Å, 1.8−4.3 Å, and 1.8−5.3 Å. NOE-restrained distances involving multiple atoms at one end of the restraint, such as aromatic protons on Phe, methyl protons, or methylene groups with stereospecific assignments, were averaged for NOE calculations as the inverse sixth power of the relevant distances. The proximities of the side chains of residues Met24, Glu25, Asp67, Leu70, and Leu71 to the metal cluster, as indicated by paramagnetic broadening, were used as weak structural restraints. Based on calculations performed for *Anabaena* ferredoxin (*36*), it was assumed for Tdx that ^{1}H resonances that are broadened to invisibility are at a maximum distance of ca. 8 Å to the iron atoms of the cluster. Because of the ambiguity as to which iron gives rises to broadening, broadened ^{1}H resonances (NH and $C_\epsilon H_3$ of Met24, NH of Glu25, C_αH of Glu67, two methyl groups of Leu70, and two methyl groups of Leu71) were restrained to 8 Å distance to both irons with an allowed ±3 Å deviation without energetic penalty.

The use of backbone dihedral angle restraints significantly improves the convergence and quality of NMR-derived structures. While the measurement of ψ backbone dihedral angles (N−C_α−CO−N) by NMR methods is not straightforward, ϕ angles (CO−N−C_α−CO) can be correlated to the scalar coupling between HN and C_αH using the Karplus relation. Data from three-dimensional J_{HNHA}-resolved ^{1}H,^{15}N HSQC and HNHA experiments were combined to extract dihedral restraints on ϕ. Though the results of the two experiments give similar information, each experiment has advantages and disadvantages. For most diamagnetic residues in Tdx^o, the J_{HNHA}-resolved ^{1}H,^{15}N HSQC experiment (*31*) was satisfactory for estimating J_{HNHA}. However, for some resonances close to the edge of the paramagnetic region, no resolved splitting was apparent in the J_{HNHA} dimension, even when it was clear from NOE and other structural considerations that a large coupling might be expected. In these cases, the HNHA experiment often provided the necessary information. Moreover, J_{HNHA}-resolved ^{1}H,^{15}N HSQC does not give useful coupling information for glycines because the couplings of the two $C_\alpha H_2$ protons of Gly are not resolved. The HNHA experiment can yield stereospecific assignments for the $C_\alpha H_2$ protons of Gly in combination with data from the HNHB experiment and NOE information (*31*). J_{HNHA} couplings were separated by magnitude as large ($J > 8$ Hz), medium (8 Hz $> J >$ 6 Hz), and small ($J <$ 6 Hz): a large coupling constant corresponds to a backbone ϕ angle of 130 ± 40°; a medium one to 130 ± 60° for β-sheet residues or 70 ± 40° otherwise; a small coupling constant corresponds to 70 ± 20°. Experimental restraints on χ_1 angles used in structural calculations were determined using data from NOESY, TOCSY, DQ, and HNHB experiments. For Met94, χ_2 was also determined. For all χ angles, ±40° was allowed with no energy penalty.

Restraining Gly residues for solution structure calculations can be problematic. The presence of two $C_\alpha H_2$ protons makes stereospecific assignments and extraction of ϕ angles difficult to do unambiguously. Without angular restraints on Gly residues, however, structural calculations converge only slowly for Tdx. Two Gly residues were restrained, noting their positions in well-defined secondary structural features. Examination of NOE patterns reveals that both Gly20 and Gly80 are the third residues of type II tight turns. As such, the ϕ and ψ angles for these Gly residues were restrained to values typical of these turns. Gly11 was identified as the fourth residue of a type I turn and occupies a position homologous to residues in Adx and Pdx with positive ϕ angles, and so was thus restrained. Gly61, which breaks helix F, was restrained to a positive ϕ angle based on observed NOEs. Gly96 was also required to adopt a positive ϕ angle based on secondary structural considerations. Gly34 was restrained in the positive ϕ angle region. However, dihedral angles for Gly31 and Gly75 were not restrained, as either positive or negative ϕ angles for these residues can lead to convergent structures.

Modeling of the Fe_2S_2 Binding Site. Paramagnetism arising from the Fe_2S_2 cluster broadens nuclear spin resonances near the metal binding site of Tdx^o. This prevents the sequential assignment of ^{1}H resonances or the use of extensive

FIGURE 4: Stereoview of the backbone superposition of the family of 15 superimposed backbone Tdx^{o} structures described here. The view is approximately the same as that in Figure 5. The family of structures exhibits an RMSD of 1.3 Å for backbone atoms and 1.8 Å for all heavy atoms. If the metal binding site and loop (residues Val36−Arg49 and Leu84−Gln87) and the C-terminus (residues 102−105) are removed from the calculation, the backbone/heavy atom RMSD improves to 0.9 and 1.6 Å, respectively.

experimental restraints for structure calculations in this region of the protein. To calculate a complete structure for Tdx^{o}, it was necessary to provide a rational model for those regions of the protein for which NOEs and dihedral angle restraints cannot be directly determined. As for the Pdx^{o} structure calculations (*7*, *8*), the Fe$_2$S$_2$ cluster was modeled using bond distances, bond angles, and dihedral angles for the cluster and cysteine ligands obtained from a ferredoxin crystal structure, in this case the recently published structure for bovine Adx (*9*) with Cys39 and Cys48 ligating to Fe1 and Cys46 and Cys86 ligating to Fe2. Backbone dihedral angles were constrained (±20°) for residues in the metal binding loop and near the fourth cysteine ligand (residues Glu38−Arg49, and Leu84−Gln87) using the observed dihedral angles for the corresponding residues in Adx. Ile35, Val36, and Ala37 were left unrestrained in this fashion, as the counterpart of Ala37 in Adx is a Gly residue that exhibits a positive ϕ angle.

The validity of this approach to the modeling of ferredoxin metal binding sites was demonstrated by the after-the-fact observation that the metal clusters of Pdx and Adx almost precisely superimpose in best-fit backbone alignments of the NMR-derived solution structure of Pdx^{o} and the crystal structure of Adx (*9*). A complete list of modeling constraints on the metal cluster and environs is given in Table 2.

Features of the Solution Structures. A family of 15 superimposed structures of Tdx^{o} are shown in Figure 4. The chosen structures were selected from over 100 candidate structures based on the absence of NOE violations >0.5 Å and dihedral angle violations >5°. Furthermore, chosen structures exhibit few Ramachandran outliers as calculated by PRO_CHECK_NMR (*37*). For all 15 structures, 63.9% of nonglycinyl and nonprolyl backbone dihedral angles lie in the most favored regions, and 34.0% lie in the additional allowed regions. Only 1.8% are found in the generously allowed regions, and 0.2% in the disallowed regions. The family of structures shown exhibits an RMSD for backbone atoms of 1.3 Å and for all heavy atoms of 1.8 Å. If the metal binding site and loop (residues Val36 to Arg49 and Leu84 to Gln87) and the C-terminus (residues 102−105) are removed from the calculation, the backbone/heavy atom RMSD improves to 0.9 and 1.6 Å, respectively. As was noted previously for the Pdx^{o} structure (*7*), the low positional precision of helix G relative to the rest of the structure is likely to be an artifact of the relative paucity of NOE restraints between the helix and residues near the metal center than true motional freedom.

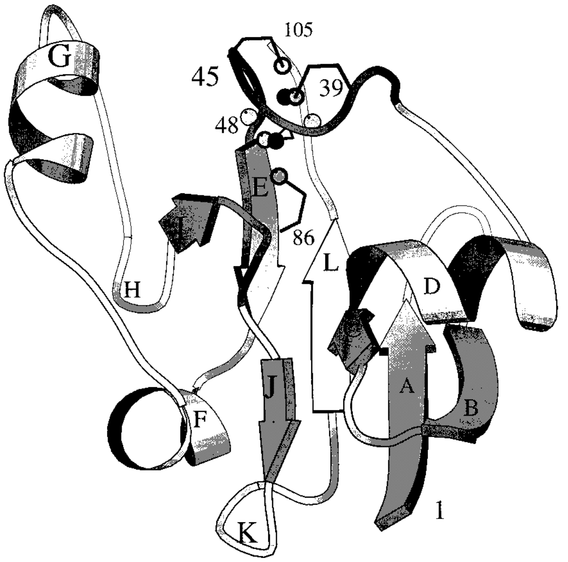

FIGURE 5: Ribbon plot of Tdx structure. Residues corresponding to each domain are strand A (Pro1−Asp7), strand B (Glu12−Ala17), strand C (Gln21−Ser22), helix D (Leu23−Asn30), strand E (Ile50−Glu53), helix F (Ala55−Val60), helix G (Pro65−Ser73), turn H (Thr79−Thr82), strand I (Thr82−Arg83), strand J (Val88−Ile90), turn K (Asp91−Met94), and strand L (Leu97−Val101). The iron atoms in the metal cluster are shown as dark spheres, the inorganic sulfide atoms as lighter spheres with thin borders, and the cysteinyl sulfurs as lighter spheres with thick borders. The carbon−carbon and carbon−sulfur bonds of the four cysteinyl ligands (Cys39, Cys45, Cys48, and Cys86) are also shown and numbered. The C- and N-termini are also numbered. Residues in the metal binding loop region (shown darker) have no NMR assignments and so were modeled using the Adx crystal structure (*9*). The figure was generated using MOLSCRIPT (*57*).

Two β-sheets are identified in Tdx, a large five-stranded sheet and a smaller two-stranded sheet (Figure 5). The larger sheet is composed of antiparallel strands A (Pro1, Arg2, Val3, Val4, Phe5, Asp6, Ile7) and B (Asp12, Tyr13, Ala14, Val15, Asp16, and Ala17). Strand L (Leu97, Ile98, Val99, Arg100, Val101) parallels strand A but is antiparallel to strand E (Ile50, Glu51, Ile52). A short fifth strand I (Thr82 and Arg83) is antiparallel to strand E. The smaller sheet consists of the two short antiparallel strands C (Gln21, Ser22) and K (Val88, Phe89, and Ile90). As is often observed, many of the NH protons in both sheets show significant protection from solvent exchange. All of the NH protons in strand A, embedded as it is in the β-sheet network, are protected from fast H/D exchange. Strand B is at one edge of the sheet, and so only every other residue's backbone amide proton is protected from fast exchange.

Three helices have been identified in Tdx (Figure 5) via characteristic sequential and near-residue NOEs. The first, helix D, includes residues Leu23−Gln29. Met24 and Glu25, both in helix D, are in proximity to the metal cluster, based on structure homology and the observed broadening of their ^{1}H resonances. The δ-sulfur atom of Met24 may act in some fashion to modulate the redox behavior of the iron−sulfur cluster, since the δ-sulfur of the corresponding Met24 in Pdx is in close proximity to the metal center in the diamagnetic gallium derivative of Pdx, GaPdx. However, the function of this residue has not yet been examined by mutagenesis. The second helix, F, is formed by residues Asp54−Val60, while the third helix, G, consists of residues Pro65−Ser73. Helix G also contains some paramagnetically broadened residues, including Glu67, Leu70, and Leu71, indicating the proximity of the helix to the metal cluster.

Three tight turns were identified by characteristic NOE patterns in the Tdx structure, all of which contain glycine. Residues Gln18−Gln21 and residues Thr79−Thr82 form type II tight turns, with glycines (Gly20 and Gly81) as third residues. Residues Glu8−Gly11 form a type I turn between strands A and B of the large β-sheet.

As is the case for both Pdx (*7, 8*) and Adx (*9*), the structure of Tdx^o consists of two primary domains (Figure 5). The first of these two domains consists of the major hydrophobic core of the protein. The side chains of residues Val3, Phe5, Tyr13, Val15, Ala17, Ile50, Ile52, Leu97, Val99, and Val101 from the large β-sheet all contribute to forming the hydrophobic core of Tdx^o. Also involved in the core are the side chains of residues Gln21 and Ile90 from the smaller β-sheet, the side chains of Leu23, Val26, Ala27, and Thr28 from helix D, and the indole of Trp56 from helix F. This domain resembles similar core domains in Pdx, Adx, and plant ferredoxins for which structures have been determined.

Two aromatic residues provide nucleation for the hydrophobic core of Tdx. The indole of Trp56, located on helix F, provides tertiary contacts with residues in the tight turn K and strand L. Leu97 and Ile98 on strand L are in close proximity to Trp56's indole ring, as indicated by strong NOEs to indole resonances and the large upfield shifts of Leu97 C_αH (0.98 ppm) and the NH of Ile98 (4.79 ppm). A very similar shift pattern is seen for Ile97 and Val98 in Pdx (*33*). Assignment of the C_αH of Leu97 is supported by the natural-abundance ^{1}H,^{13}C HSQC spectrum, which shows a correlation between the C_αH of Leu97 (0.98 ppm) and an unperturbed $^{13}C_\alpha$ with a chemical shift at 55.2 ppm (H. Mo, unpublished results). The ^{1}H,^{15}N HSQC correlation between the C_αH (4.56 ppm) and NH of Ile98 (4.79 ppm) is readily observed in D_2O, since the Ile98 NH is protected from exchange by virtue of its position within the β-sheet. Phe5 also provides important contacts for residues in the hydrophobic core of Tdx. The side chains of Ala27 and Val32 both exhibit NOEs and ring current shifts from the Phe5 aromatic ring, fixing the position of helix D and the preceding polypeptide relative to the large β-sheet.

The second domain of the Tdx structure is formed by a series of polar and hydrophobic interactions involving the side chains of residues Arg49, Glu51, Glu67, Leu70, Leu71, Glu74, Pro77, Met78, Thr82, Arg83, and Leu84. Arg49 and Glu51 project from the "back" face of the large β-sheet (strand E), as do residues Thr82 and Leu84 (strand L). Residues Asp67, Leu70, and Leu71 are found on the interior side of helix G, and residues Pro77 and Met78 are on a strand that links helix G to type II turn H. This domain has an analogue in the Pdx structure in the form of the C-terminal cluster, which we described in detail previously (*37*). A similar domain has also described in the Adx crystal structure, and was termed the interaction domain by those researchers, in light of the considerable importance of surface residues in this region to the binding of cognate cytochrome P450s (*9*).

The Fe_2S_2 cluster binding site lies between the two domains of Tdx. The side chains of Glu67, Leu70, Leu71, and Leu84 are broadened by proximity to the metal cluster, as are the side chains of Met24 and Glu25. If the GaPdx solution structure (38) and Adx crystal structure are reasonable guides, the side chains of residues Met24, Leu70, and Leu84 also interact directly with the metal center, and may provide structural stability for the cluster. They may also be involved functionally in transmitting any redox-dependent changes in protein structure and dynamics at the metal center to the rest of the protein.

Limitations on the Model. The structures shown in Figure 4 were determined solely from distance and dihedral restraints, along with bond lengths, bond angles, and hard-sphere van der Waals interactions. No explicit hydrogen bonding or electrostatic terms were used in the calculations. As such, the structures are biased toward conformations favored by the given NOE and dihedral angle restraints. The lower precision observed in the Tdx structures for coordinates in regions for which NOE data are limited due to paramagnetic relaxation, (e.g., helix G and the following loop) is probably an artifact of the lack of NOEs restraining the helix relative to the metal cluster binding site. Furthermore, in regions where paramagnetism precludes the use of any but the most general experimental restraints, there is no good estimate for the accuracy of the artificial restraints used to model the structure. As such, details of the Tdx structure in the vicinity of the metal binding site should not be overinterpreted.

H/D Exchange as a Function of Structure and Oxidation State. Amide proton exchange rates were determined for Tdx by measuring the rate at which peak intensity is lost in ^{1}H,^{15}N HSQC spectra after exchanging the sample of Tdx into deuterated buffer, using a procedure identical to that described for similar experiments on Pdx (*32*). Those rate constants that could be measured by this method are available as Supporting Information. Qualitatively, solvent accessibility for various residues could be estimated after a relatively short exchange period (15 min) by examination of the ^{1}H,^{15}N HSQC spectrum. All side chain amide protons of Gln and Asn were found to be accessible to the solvent and serve as a standard for fast exchange.

Exchange rates for nominally exchangeable protons provide evidence for solvent exposure of particular residues. For example, hydroxyl protons in proteins tend to exchange with solvent very rapidly and are not usually detectable by NMR. However, hydrogen bonding involving the OH group within the protein interior can protect the hydroxyl proton

FIGURE 6: Stereoview of the backbone superposition of one of the family of Tdx^o structures described here (heavy lines) onto the backbone coordinates of the crystallographic structure of adrenodoxin, shown in light lines (Adx) (9). The view is approximately the same as that in Figure 5. The structures exhibit an RMSD of 2.54 Å.

from exchange, making it possible to detect the OH resonance under some circumstances. The OH of Ser22 on strand C is observable in 2D NMR spectra of Tdx^o. Extensive intraresidue and interresidue NOEs were found to support this assignment. Based on NOEs, the Ser22 OH is likely hydrogen-bonded to the Glu25 side chain carbonyl oxygen.

The side chains of Arg2 and Arg100, both in the large β-sheet, are solvent-exposed, and their guanidinium NH_2 protons are not observed. In contrast, the side chains of Arg49 and Arg83 are both internal, with little or no solvent exposure for their guanidinium groups. Broadened terminal guanidinium NH_2 proton resonances were observed for both of these residues. Based on the position of its side chain, Arg83 guanidinium NH_2 groups likely form hydrogen bonds (or a salt bridge) with the carboxylate of Glu62, and there are several potential hydrogen bond acceptors near the guanidinium group of Arg49.

The two separate domains of Tdx described above exhibit considerably different dynamics as determined by amide proton exchange. The large hydrophobic core domain is compact, with many interresidue NOEs observed between the component side chains. H/D exchange is slow for amides within this region. On the other hand, the second domain appears to be more mobile, with a greater degree of solvent accessibility. Only a few backbone amides experience slow exchange in this region (Leu70, Leu71).

Amide proton exchange rates have also been measured for reduced Tdx (Tdx^r) to allow comparison with the oxidized form. Like Pdx and human ferredoxin (which is highly homologous to bovine Adx), Tdx shows slowing of amide proton exchange for helical region G upon reduction (H. Mo, unpublished results). The extent of the exchange rate differences between oxidized and reduced Tdx^o is considerably less than for Pdx or, based on published evidence, than for Adx (*32, 39*).

DISCUSSION

The Tdx structure is now the third structure to be solved for the structurally distinct class of Fe_2S_2 ferredoxins that transfer electrons to cytochromes P450. The three structures (Pdx^o, Adx, and Tdx^o) all show considerable similarity in global fold and arrangements of the two domains (Figure 6). The hydrophobic core domains of the three proteins in particular are very similar, both to each other and to the core domains of other ferredoxins for which structures have been determined. However, it is significant that these three ferredoxins do not substitute efficiently for each other in their respective hydroxylase systems, suggesting that there are specific structural features responsible for proper bonding and/or electron transfer between the ferredoxins and their cognate cytochromes (*4*, *40*, *41*). Progress has been made in identifying structural features of Pdx critical for activity (*42*−*45*) and Adx (*12*, *46*−*48*). It is apparent from published data that CYP101 binds Pdx differently than CYP11A1 binds Adx. Published models and experimental results implicate several acidic residues in the metal cluster binding loop in the interaction between Pdx and CYP101 (*42*, *43*, *49*). In turn, specific arginine residues on CYP101 have been identified as important for binding Pdx (*50*, *51*). Interestingly, several lysine residues on CYP11A1 without homology in the sequence of CYP101 have been found to be critical for binding Adx (*52*), while the acidic residues Asp72, Asp76, and Asp79 on the helix in Adx corresponding to helix G of Pdx are identified as contributing to the binding of CYP11A1. The acidic residues of helix G in Pdx do not appear to affect binding to CYP101 (*43*).

Nothing is known as yet about specific residues on Tdx that are involved in binding CYP108. As noted above, Pdx and Tdx do not substitute particularly well for each other in their respective enzyme systems. These observations are not surprising, in that the most prominent structural differences between Tdx and Pdx are to be found in the C-terminal domain in Pdx, which has been implicated in CYP101 binding. The C-terminal peptide in Pdx (Asp103−Trp106) is well-defined, with many NOEs from the C-terminus, particularly Trp106, to other residues in the C-terminal cluster domain. Trp106 was identified some time ago as critical for the biological activity of Pdx (*53*). Deletion or replacement of Trp106 in Pdx by a nonaromatic residue results in a severe reduction in binding between Pdx and CYP101 (*54*). The ^{1}H chemical shifts for the C-terminal residues in Tdx are close to random coil shifts, and do not exhibit nonsequential NOEs. In this respect, Tdx resembles Adx more than it does Pdx. The C-terminal peptide past Pro108 at the C-terminus of β-strand L shows no evidence of structure in oxidized Adx (*39*), and the des-109 mutant of Adx, in which all residues past Pro108 have been deleted, is fully functional (*46*).

Other differences between Tdx and both Pdx and Adx are found in the second domain, as well. One of the most striking is the absence of a His residue in Tdx at position 49. Both Pdx and Adx have His residues at this position (His49 in Pdx, His56 in Adx) while Tdx has an arginine. The His residue is unprotonated in both Pdx and Adx at physiological pH, and does not titrate over any accessible pH range in either protein (*55*, *32*). A hydrogen bonding network involving His49 (His56 in Adx) and other nearby residues in the second domain is suggested by ^{1}H chemical shifts and exchange behavior in Pdx (*37*) and is demonstrated in the crystal structure of Adx where His56 hydrogen bonds to Tyr82 and Ser88 (*9*).

We have suggested that the redox-dependent amide exchange rates exhibited in the C-terminal region of Pdx (*32*) are due in large part to modulation of polar interactions (i.e., hydrogen bond strength) by changes in charge at the metal cluster (*56*). Evidence exists for considerable redox dependence of amide exchange rates for residues near the metal center in Adx as well (*38*, *39*), although no residue-specific measurements have been published as yet for that protein. We have measured relative H/D exchange in Tdx^o and Tdx^r, and although some changes of H/D exchange rates are observed upon reduction of Tdx, the overall effect of reduction upon amide exchange rates is much less than for Pdx (or, presumably, for Adx). In the C-terminal domain, Asp69 moves from the fast exchange regime in Tdx^o to slow exchange in Tdx^r. Exchange of the NH of Gly61 also slows down upon reduction, and exchange rates for the NH protons of Leu70 and Leu71 are significantly slower ($10\times$) in Tdx^r than in Tdx^o. However, in no case do these values approach some of the larger changes in exchange rate that have been observed for Pdx in the C-terminal cluster (some NH exchange rates being greater than 80 times faster in Pdx^o than in Pdx^r) or those that might be expected in Adx based on published observations.

It is possible that the substitution of Arg for His at position 49 is responsible at least in part for the lessened dependence of local dynamics on oxidation state in Tdx relative to Pdx and (presumably) Adx. As proposed elsewhere (*9*), the position of this residue immediately adjacent to the cysteine ligand Cys48 puts it in an ideal position to mechanically transmit any structural or dynamic changes that occur at the metal cluster to nearby residues in the second domain to which the side chain of residue 49 is hydrogen bonded. Like His49 in Pdx and His56 in Adx, Arg49 likely takes part in a hydrogen bonding network in the second domain. The guanidinium protons of Arg49 are in slow exchange with solvent, an observation that supports this notion. However, the increased flexibility of the arginine side chain relative to that of histidine may weaken the mechanical coupling between the metal binding site and the second domain, thus dampening out the mechanical transmission of any perturbations of the metal cluster binding site due to a change in oxidation state.

ACKNOWLEDGMENT

We thank Prof. Julian A. Peterson (University of Texas Southwestern Medical Center) for providing us with preliminary samples of Tdx^o and the original Tdx gene, Huiling Gong for access to her activity assay data, Melissa Heinsen for access to her mass spectral data on recombinant Tdx, and Dr. Jürgen Müller (Max Delbruck Institute, Berlin) for access to the crystallographic coordinates of bovine adrenodoxin.

SUPPORTING INFORMATION AVAILABLE

^{1}H and ^{15}N chemical shifts for the diamagnetic regions of Tdx^o as well as measured amide proton exchange rates are available as Supporting Information (7 pages). This material is available free of charge via the Internet at http://pubs.acs.org.

REFERENCES

1. Cushman, D. W., Tsai, R. L., and Gunsalus, I. C. (1967) *Biochem. Biophys. Res. Commun. 26*, 577−583.
2. Peterson, J. A., Lu, A.-P., Geisseisoder, J., Graham-Lorence, S., Carmona, C., Witney, F., and Lorence, M. C. (1992) *J. Biol. Chem. 267*, 14193−14203.
3. Fruetel, J. A., Mackman, R. L., Peterson, J. A., and Ortiz de Montellano, P. R. (1994) *J. Biol. Chem. 269*, 28815−28821.
4. Petserson, J. A., and Graham-Lorence, S. E. (1995) *Cytochrome P450: Structure, Mechanism and Biochemistry*, 2nd ed., pp 151−180, Plenum Press, New York.
5. Poulos, T. L., Finzel, B. C., and Howard, A. J. (1987) *J. Mol. Biol. 195*, 687−700.
6. Hasemann, C. A., Ravichandran, K. G., Peterson, J. A., and Deisenhofer, J. (1994) *J. Mol. Biol. 236*, 1169−1185.
7. Pochapsky, T. C., Ye, X. M., Ratnaswamy, G., and Lyons, T. A. (1994) *Biochemistry 33*, 6424−6432.
8. Pochapsky, T. C., Jain, N., Kuti, M., Lyons, T. A., and Heymont, J. (1999) *Biochemistry 38*, 00000.
9. Müller, A., Müller, J. J., Muller, Y. A., Uhlmann, H., Bernhardt, R., and Heinemann, U. (1998) *Structure 6*, 269−280.
10. Studier, F. W., Rosenberg, A. H., Dunn, J. J., and Dubendorff, J. W. (1990) *Methods Enzymol. 185*, 60−89.
11. Sambrook, J., Fritsch, E. F., and Maniatis, T. (1989) *Molecular Cloning: a Laboratory Manual*, 2nd ed., Cold Spring Harbor Laboratory Press, Cold Spring Harbor, NY.
12. Coghlan, V. M., and Vickery, L. E. (1991) *J. Biol. Chem. 266*, 18606−18612.
13. Jacobson, B. L., Chae, Y. K., Böhme, H., Markley, J. L., and Holden, H. M. (1992) *Arch. Biochem. Biophys. 294*, 279−281.
14. Chae, Y. K., Xia, B., Cheng, H., Oh, B.-H., Skjeldahl, L., Wrestler, W. M., and Markley J. L. (1995) *Nuclear Magnetic Resonance of Paramagnetic Macromolecules*, pp 297−317, Kluwer Academic Publishers, Dordrecht, The Netherlands.
15. Wishart, D. S., Bigam, C. G., Yao, J., Abildgaard, F., Dyson, H. J., Oldfield, E., Markley, J. L., and Sykes, B. D. (1995) *J. Biomol. NMR* 6, 135−140.
16. Marion, D., and Wuthrich, K. (1983) *Biochem. Biophys. Res. Commun. 113*, 967−974.
17. Marion, D., Ikura, M., Tschudin, R., and Bax, A. (1989) *J. Magn. Reson. 85*, 393−399.
18. Piatini, U., Sørenson, O. W., and Ernst, R. R. (1982) *J. Am. Chem. Soc. 104*, 6800−6801.
19. van Zijl, P. C. M., Johnson, M. O., Mori, S., and Hurd, R. E. (1995) *J. Magn. Reson. A 113*, 265−270.
20. Jeener, J., Meier, B. H., Bachmann, P., and Ernst, R. R. (1979) *J. Chem. Phys. 71*, 4546−4553.
21. Grzesiek, S., and Bax, A. (1993) *J. Am. Chem. Soc. 115*, 12593−12594.
22. Piotto, M., Saudek, V., and Sklenar, V. (1992) *J. Biomol. NMR 2*, 661−665.
23. Sklenar, V., Piotto, M., Leppik, R., and Saudek, V. (1993) *J. Magn. Reson. A 102*, 241−245.
24. Davis, D. G., and Bax, A. (1985) *J. Am. Chem. Soc. 107*, 2820−2821.
25. Rance, M., Chazin, W. J., Dalvit, C., and Wright, P. E. (1989) *Methods Enzymol. 176*, 114−134.
26. Shaka, A. J., Lee, C. J., and Pines, A. (1988) *J. Magn. Reson. 77*, 547−552.

27. Bodenhausen, G., and Reuben, D. J. (1980) *Chem. Phys. Lett. 69*, 185−188.
28. Lippens, G., Dhalluin, C., and Wieruszeski, J. M. (1995) *J. Biomol. NMR 5*, 327−331.
29. Vuister, G. W., and Bax, A. (1992) *J. Magn. Reson. 98*, 428−433.
30. Kuboniwa, H., Grzesiek, S., Delaglio, F., and Bax, A. (1994) *J. Biomol NMR 4*, 871−878.
31. Dux, P., Whitehead, B., Boelens, R., Kaptein, R., and Vuister, G. W. (1997) *J. Biomol. NMR 10*, 301−306.
32. Lyons, T. A., Ratnaswamy, G., and Pochapsky, T. C. (1996) *Protein Sci. 5*, 627−639.
33. Ye, X. M., Pochapsky, T. C., and Pochapsky, S. S. (1992) *Biochemistry 31*, 1961−1968.
34. Williams, J. G., and Gratzer, W. B. (1971) *J. Chromatogr. 57*, 121−125.
35. Vidakovic, M., Fraczkiewicz, G., Dave, B. C., Czernuszewicz, R. S., and Germanas, J. P. (1995) *Biochemistry 34*, 13906−13913.
36. Oh, B. H., and Markley, J. L. (1990) *Biochemistry 29*, 3993−4004.
37. Laskowski, R. A., Rullmann, J. A., MacArthur, M. W., Kaptein, R., and Thornton, J. M. (1996) *J. Biomol. NMR 8*, 477−486.
38. Orme-Johnson, N. R., Mims, W. B., Orme-Johnson, W. H., Bartsch, R. G., Cusanovich, M. A., and Peisach, J. (1983) *Biochim. Biophys. Acta 748*, 68−72.
39. Xia, B., Volkman, B. F., and Markley, J. L. (1998) *Biochemistry 37*, 3965−3973.
40. Geren, L. M., Tuls, J., O'Brien, P., Millett, F., and Peterson, J. A. (1986) *J. Biol. Chem. 261*, 15491−15495.
41. Lipscomb, J. D., Sligar, S. G., Namtvedt, M. J., and Gunsalus, I. C. (1976) *J. Biol. Chem. 251*, 1116−1124.
42. Pochapsky, T. C., Lyons, T. A., Kazanis, S., Arakaki, T., and Ratnaswamy, G. (1996) *Biochimie 78*, 723−733.
43. Holden, M., Mayhew, M., Bunk, D., Roitberg, A., and Vilker, V. (1997) *J. Biol. Chem. 272*, 21720−21725.
44. Roitberg, A. E. (1997) *Biophys. J. 73*, 2138−2148.
45. Aoki, M., Ishimori, K., Morishima, A., and Wada, Y. (1998) *Inorg. Chim. Acta 272*, 80−88.
46. Uhlmann, H., Iametti, S., Vecchio, G., Bonomi, F., and Bernhardt, R. (1997) *Eur. J. Biochem. 248*, 897−902.
47. Beckert, V., Dettmer, R., and Bernhardt, R. (1994) *J. Biol. Chem. 269*, 2568−2573.
48. Beckert, V., Schrauber, H., Bernardt, R., Van Dijk, A. A., Kakoschke, C., and Wray, V. (1995) *Eur. J. Biochem. 231*, 226−235.
49. Coghlan, V. M., and Vickery, L. E. (1992) *J. Biol. Chem. 267*, 8932−8935.
50. Stayton, P. S., and Sligar, S. G. (1990) *Biochemistry 29*, 7381−7386.
51. Nakamura, K., Horiuchi, T., Yasukochi, T., Sekimizu, K., Hara, T., and Sagara, Y. (1994) *Biochim. Biophys. Acta 1207*, 40−48.
52. Wada, A., and Waterman, M. R. (1992) *J. Biol. Chem. 267*, 22877−22882.
53. Sligar, S. G., Debrunner, P. G., Lipscomb, J. D., Namtvedt, M. J., and Gunsalus, I. C. (1974) *Proc. Natl. Acad. Sci. U.S.A. 71*, 3906−3910.
54. Davies, M. D., and Sligar, S. G. (1992) *Biochemistry 31*, 11383−11389.
55. Xia, B., Cheng, H., Skjeldahl, L., Coghlan, V. M., Vickery L. E., and Markley, J. L. (1995) *Biochemisty 34*, 180−187.
56. Pochapsky, T. C., Arakaki, T., Jain, N., Kazanis, S., Lyons, T. A., Mo, H., Ratnaswamy, G., and Ye, X. (1998) in *Structure, Motion, Interaction and Expression of Biological Macromolecules* (Sarma, R. H., and Sarma, M. H., Eds.) pp 79−89, Adenine Press, Guilderland, NY.
57. Kraulis, P. J. (1991) *J. Appl. Crystallogr. 24*, 946−950.
58. Needleman, E. S., and Wunsch, D. C. (1970) *J. Mol. Biol. 48*, 443−453.

BI983063R